Journal of Energy Chemistry 115 (2026) 151–158

Contents lists available at ScienceDirect

Journal of Energy Chemistry

journal homepage: www.elsevier.com/locate/jechem

http://www.journals.elsevier.com/journal-of-energy-chemistry/

Overcoming optical/electrical losses in ultra-thin PEDOT:PSS-based interconnecting layers for efficient tandem solar cells

Bing Guo [a], Ruihan Wu [b], Senyao Wang [b], Jiaqi Li [a], Bin Kan [c], Zhaoyang Yao [a], Xiangjian Wan [a], Chenxi Li [a], Lei Meng [b], Yongfang Li [b,d], Yongsheng Chen [a,*]

[a] State Key Laboratory and Institute of Elemento-Organic Chemistry, The Centre of Frontiers Science Center for New Organic Matter, Nanoscale Science and Technology and Key Laboratory of Functional Polymer Materials, Renewable Energy Conversion and Storage Center (RECAST), College of Chemistry, Nankai University, Tianjin 300071, China
[b] CAS Key Laboratory of Organic Solids, Institute of Chemistry, Chinese Academy of Sciences, Beijing 100049, China
[c] School of Materials Science and Engineering, National Institute for Advanced Materials, Nankai University, Tianjin 300350, China
[d] Laboratory of Advanced Optoelectronic Materials, College of Chemistry, Chemical Engineering and Materials Science, Soochow University, Suzhou 215123, Jiangsu, China

ARTICLE INFO

Article history:
Received 15 September 2025
Revised 23 October 2025
Accepted 11 November 2025
Available online 24 November 2025

Keywords:
Tandem solar cells
PEDOT:PSS
Interconnecting layer
Transmittance
Doping

ABSTRACT

The interconnecting layer (ICL) plays a critical role in series-connected tandem solar cells (TSCs). However, the PEDOT:PSS layer, commonly used hole transport layer in ICL, still exhibits non-negligible light absorption, which remains an obstacle to further improve the photovoltaic performance of TSCs. Here, we demonstrate an efficient strategy to mitigate optical and electrical losses in PEDOT:PSS-based ICLs by reconstructing PEDOT:PSS film via alkali metal carbonate (AMC) doping. AMC doping can increase the proportion of PEDOT in PEDOT:PSS thin films, allowing them to be ultra-thin but robust enough to isolate adjacent active layers. Comprehensive characterizations demonstrate that AMC doping promote increased transmittance, decreased resistance and optimized surface morphology for PEDOT:PSS films. As a result, both the short-circuit current density (J_{sc}) and power conversion efficiency (PCE) are improved after AMC doping in PEDOT:PSS for TSCs with different active layer combinations, exhibiting excellent universality in TSCs application. Notably, the PCEs of organic homo-TSCs and perovskite/organic TSCs with AMC doping reached 20.04 % and 26.05 %, respectively. Our work underscores the great potential of AMC doping in optimizing PEDOT:PSS films in ICL, offering an innovative pathway for fabricating highly efficient TSCs.

1. Introduction

Tandem solar cells (TSCs) are considered as a promising solution to overcome the efficiency limitation in single-junction solar cells owing to significantly suppressed transmission and thermalization losses [1–5]. According to Shockley and Queisser's calculation, a single-junction solar cell can only convert 30 % of the solar energy under 1 sun irradiance, while a tandem solar cell combined with two cells can convert 42 % [6,7]. Typically, TSCs are composed of three parts, including the front subcell, rear subcell and interconnecting layer (ICL) that establishes electrical contact between the two subcells. The ICL, basically consisting of hole transport layer (HTL) and electron transport layer (ETL), enables the collection of photogenerated charge carriers from the subcells and facilitates their efficient recombination, which plays a critical role in TSCs. An ideal ICL should meet several critical requirements, including physical/chemical robust, high optical transmittance, sufficient electrical conductivity, etc. [5].

Among these various ICLs, the combination of metal oxide (ZnO and SnO_x) as ETL and poly(3,4-ethylenedioxythiophene):poly(styrenesulfonate) (PEDOT:PSS) as HTL remains a widely adopted choice in not only organic/organic TSCs, but also perovskite-related tandem photovoltaics (perovskite/perovskite, perovskite/organic and perovskite/silicon TSCs) [2,4,8]. Beyond the most fundamental robust barrier requirement, high optical transmittance and sufficient electrical conductivity are very important. Ultra-thin metal layers [9–19] are sometimes used inside ICLs to facilitate efficient recombination, while they exhibit severe parasitic light absorption and lead to current reduction. It has been reported that some transparent conductive oxides (such as ITO or IZO) [20–22] and

* Corresponding author.
E-mail address: yschen99@nankai.edu.cn (Y. Chen).

https://doi.org/10.1016/j.jechem.2025.11.024

graphene-oxide [23] recombination layers can significantly reduce optical losses and lead to an effective ohmic contact for carrier transport in TSCs. To increase the electrical conductivity of PEDOT:PSS, acid doping [24] and self-assembled monomer [16,25] modify have been established to improve the hole collection and transport. Despite much effort has been devoted to the optimization of ICLs, optical losses are still existed and limit the current performance of TSCs. Compared with highly transparent (even with anti-reflection property) metal oxide ETLs, the PEDOT:PSS layer still exhibits non-negligible light absorption in the visible and near-infrared region. However, few studies have been reported on improving the transmittance of the PEDOT:PSS layer in ICLs.

In this study, we report an alkali metal carbonate (AMC) doping strategy in PEDOT:PSS to improve its transmittance and the corresponding efficiency of TSCs. It is found that AMC doping can optimize the composition of PEDOT:PSS films, making the optimal film thickness become thinner and thus improving the transmittance. Higher PEDOT content enables the film to remain sufficiently robust to block solvent penetration even at a very thin thickness. Moreover, doped PEDOT:PSS films show decreased resistance, which is beneficial for charge transport. As a result, both the short-circuit current density (J_{sc}) and power conversion efficiency (PCE) are improved after AMC doping in PEDOT:PSS for TSCs with different active layer combinations. Notably, the PCEs of organic homo-TSCs and perovskite/organic TSCs with AMC doping reached 20.04 % and 26.05 %, respectively. These findings demonstrate that AMC doping has great potential for optimizing PEDOT:PSS films in ICLs.

2. Experimental

2.1. Materials

PM6 was purchased from Hyper, Inc. L8-BO and BTP-eC9 was purchased from Solarmer Material. CH22 was synthesized according to the reported work [26]. (2-(9H-carbazol-9-yl)ethyl)phosphonic acid (2PACz) was purchased from Hyper, Inc. Fluorine-doped tin oxide (FTO) glass, indium tin oxide (ITO) glass, formamidinium iodide (FAI), methylammonium iodide (MAI), lead iodide (PbI_2, 99.999 %), lead bromide ($PbBr_2$, 99.999 %) and (4-(7H-dibenzo[c,g]carbazol-7-yl)butyl) phosphonic acid (4PADCB) were purchased from Advanced Election Technology. Lead sulfocyanide [$Pb(SCN)_2$], rubidium iodide (RbI, 99.9 %), N,N-dimethylformamide (DMF, 99.8 %), and dimethyl sulfoxide (DMSO, anhydrous) were purchased from Sigma-Aldrich. Isopropanol (IPA, 99.5 %) and ethyl acetate (EA, 99.9 %) were purchased from J&K Scientific. Poly(3,4-ethylenedioxythiophene):poly(styrene sulfonate) (PEDOT:PSS) was purchased from Heraeus. C_{60} was purchased from Leyan, Shanghai, China. 2,9-Dimethyl-4,7-diphenyl-1,10-phenanthroline (BCP) was purchased by Xi'an Yuri Solar. Silver (99.999 %) and gold (99.999 %) were purchased from ZhongNuo Advanced Material (Beijing). All chemicals and other regents, unless otherwise specified, were directly used without further purification.

2.2. Fabrication of organic homo-TSCs

First, ITO-coated glasses were sequentially cleaned by sonication with detergent, deionized water, acetone and isopropanol for 20 min, respectively. Second, the surface of ITO-coated glass was treated in an ultraviolet-ozone chamber for 20 min. For PM6:CH22-based homo-TSCs, a thin layer of PEDOT:PSS was deposited on the ITO substrate at 4300 r min^{-1} for 20 s and then dried at 150 °C for 15 min in ambient air. For the other two homo-TSCs, a thin layer of 2PACz (0.3 mg mL^{-1} in methanol) was deposited on the ITO substrate at 4000 r min^{-1} for 20 s. PM6:CH22 (1:1.2 w/w) was dissolved in chloroform at the total blend concentration of 15.4 mg mL^{-1} with 0.4 % chloronaphthalene (CN) as the solvent additive. PM6:L8-BO (1:1.2 w/w) was dissolved in chloroform at the total blend concentration of 17.6 mg mL^{-1} with 0.25 % DIO as the solvent additive. PM6:BTP-eC9 (1.2:1 w/w for front cell and 1:1.2 w/w for rear cell) was dissolved in chloroform at the total blend concentration of 17.6 mg mL^{-1} with 0.5 % DIO as the solvent additive. The front and rear active layers were spun onto the coated substrate at 3000/1800 r min^{-1} for PM6:CH22-based homo-TSCs, 7000/2000 r min^{-1} for PM6:L8-BO-based homo-TSCs, and 4000/2000 r min^{-1} for PM6:BTP-eC9-based homo-TSCs. Then the films were treated with thermal annealing at 100 °C for 5 min. For the ICLs, ZnO nanoparticles methanol solution of 25 mg mL^{-1} was spin-coated on the active layer at 2000 r min^{-1} for 20 s and then diluted PEDOT:PSS (PEDOT:PSS/H_2O = 1/2.5, v/v) was spin-coated on the ZnO layer with 4000 r min^{-1} for 20 s. Subsequently, the substrate was annealed at 120 °C for 5 min in ambient air. Phosphomolybdic acid (PMA, dissolved in methanol a concentration of 1 mg mL^{-1}) was spin-coated on the substrate layer with 4000 r min^{-1} for 20 s. After the deposition of rear active layers, the methanol solution of PNDIT-F3N (1 mg mL^{-1}) with 0.5 % acetic acid was spin-coated at 3000 r min^{-1} for 20 s. Finally, Ag electrode with the thickness of 150 nm was evaporated under 1×10^{-4} Pa.

2.3. Fabrication of perovskite/organic TSCs

To prepare WBG PVK precursor ($FA_{0.7}MA_{0.2}Rb_{0.1}Pb(I_{0.5}Br_{0.5})_3$) with a concentration of 1.4 M, FAI, MAI, RbI, PbI_2, $PbBr_2$ and $Pb(SCN)_2$ were dissolved in DMF:DMSO (4:1, v/v), with a molar ratio of FAI:MAI:RbI of 0.7:0.2:0.1 and PbI_2:$PbBr_2$:$Pb(SCN)_2$ of 0.2:0.8:0.04. After stirring overnight, the solution was filtered with a 0.22 μm PTFE filter and ready for spin-coating.

The monolithic perovskite-organic TSCs were fabricated with a device architecture of Glass/FTO/4PADCB/Al_2O_3/WBG PVK/C_{60}/SnO_x/Au/PEDOT:PSS/PM6:BTP-eC9/PNDIT-F3N/Ag. The pre-patterned FTO glass substrates were sequentially cleaned by sonication with detergent, deionized water, acetone and isopropanol for 20 min, respectively. The cleaned FTO substrates were treated with ultraviolet-ozone for 25 min. Subsequently, a self-assembled monolayer (SAM) were fabricated by spin-coating the 4PADCB (0.2 mg mL^{-1} in ethanol) onto the FTO at 4000 r min^{-1} for 30 s and annealed at 120 °C for 15 min. After cooling to room temperature, a dispersion of aluminum oxide (Al_2O_3) nanoparticles was dynamically spin-coated at 4000 r min^{-1} for 30 s, followed by an annealing step at 100 °C for 5 min. Then a volume of 60 μL of the filtered perovskite solution was deposited onto the substrate and spin-coated at 5000 r min^{-1}. During the final 15 s of the spin-coating process, 200 μL of EA was quickly dripped onto the center of the perovskite film to induce rapid crystallization. The film was then annealed at 100 °C for 20 min. Next, spin-coating of *cis*-$CyDAI_2$ (at a concentration of 0.3 mg mL^{-1} in 200:1, v/v, IPA:DMF) was done onto the as-formed perovskite at 3000 r min^{-1} for 30 s, followed by annealing at 100 °C for 5 min. C_{60} (25 nm) was deposited on the perovskite layer, followed by the deposition of a 20 nm SnO_x via atomic layer deposition (ALD). After that, 1 nm Au layer was deposited by thermal evaporation at a rate of 0.1 Å s^{-1} under a vacuum of 1×10^{-4} Pa. PEDOT:PSS, which was diluted by IPA (1:3, v/v), was coated at 4000 r min^{-1} for 25 s and then heated at 120 °C for 5 min. Subsequently, the process followed the same steps as the preparation of the rear cell of PM6:BTP-eC9-based homo-TSCs. The methanol solution of PNDIT-F3N was spin-coated at 3000 r min^{-1} for 20 s. Finally, a 150-nm Ag layer was thermally evaporated under a vacuum of 1×10^{-4} Pa.

2.4. Characterization

The current density–voltage (*J-V*) curves of devices were recorded on a Keithley 2400 source-measure unit in a glove box

filled with nitrogen. Enli SS-F5-3A solar simulator with AM1.5 G was used as the light source, and the light intensity was 100 mW cm^{-2} which was calibrated by a standard Si solar cell (made by Enli Technology Co., Ltd., Taiwan, and calibrated report can be traced to NREL). The voltage step in the scan was 20 mV with a delay time of 1 ms, using a Keysight B2901A SourceMeter. The device areas determined by shadow masks were 3.24 cm^2 for homo-TSCs and 10.24 cm^2 for perovskite-organic TSCs. The EQE responses were measured using a Solar Cell Spectral Response Measurement System QE-R3-011 (Enli Technology). The light intensity at each wavelength was calibrated using a standard single-crystal Si photovoltaic cell. A Veeco Dektak 150 profilometer was used to measure the thickness of the thin layers.

UV–vis absorption and transmittance spectra were recorded on a Cary 5000 UV–vis spectrophotometer. The atomic force microscopy spectroscopy (AFM) measurements were performed on Bruker NanoIR3 by using in tapping mode. The pH values were measured by using a pH meter (BPH 7100). UPS and XPS were tested through a Kratos AXIS ULTRA DLD spectrometer. Raman spectra were tested through a WITec Alpha300 spectrometer. The cross-sectional morphology of the devices was investigated using a Hitachi S-4800. For the cross-sectional imaging, the cross-sectional surface of the sample was coated with approximately 1-nm-thick gold using sputtering to enhance conductivity.

The electrical conductivity is measured by using the device structure of Glass/ITO/PEDOT:PSS/Ag. The resistance (R) of PEDOT:PSS film can be obtained from the *J-V* curves recorded on a Keithley 2400 source-measure unit in a glove box filled with nitrogen. Electrical conductivity is the reciprocal of electrical resistivity. Resistivity (ρ) can be determined using the formula $\rho = R \times (A/L)$, where A is the cross-sectional area and L is the thickness of PEDOT:PSS film.

3. Results and discussion

The device structure of tandem solar cells used in this study is shown in Fig. 1a. The interconnecting layer (ICL) consists of ZnO or atomic layer deposition (ALD) SnO_x as electron transport layers and PEDOT:PSS as hole transport layer. To investigate the impact of PEDOT:PSS layer on the photovoltaic performance of tandem solar cells, we altered the PEDOT:PSS formulation by doping it with three distinct alkali metal carbonates (AMCs) to tune its photoelectronic properties, while maintaining all other conditions constant. Firstly, homo-tandem organic solar cells with PM6:CH22 [26] as active layer of both the front and rear cell were conducted to investigate the doping effect. The detailed tandem cell fabrication and doping process can be found in the experimental section. As shown in Fig. S1 and Table S1, when the concentration of AMCs is higher than 5 mM, all the photovoltaic parameters, including open-circuit voltage (V_{oc}), J_{sc}, fill factor (FF) and PCE, are decreased to some extent. This is primarily due to the molecular aggregation of PEDOT:PSS caused by the high AMC concentration, which can be seen from the morphology data, as will be discussed in detail later. However, the J_{sc} exhibited a particularly significant enhancement within the doping concentration range of 5 mM. At optimal doping concentration (1 mM), both the J_{sc} and PCE of AMCs doped tandem devices exhibited significant enhancement in the statistical data (Fig. 1b, c, Fig. S2 and Table 1). The J_{sc} of the tandem devices is increased by approximately 0.5 mA cm^{-2} when doping with AMCs, while the PCE rises from 18.41 % to exceeding 19 % after doping. Interestingly, there is no obvious difference on the device performance for the three different AMCs.

To gain insight into the AMC doping effect on the influence of tandem device performance, transmittance spectra were measured not only for the PEDOT:PSS layer but also the whole ICL (Fig. 2a, b and Fig. S3). At optimal AMC doping concentration of 1 mM, the transmittance of the PEDOT:PSS film was enhanced across the 350–900 nm wavelength range. A similar enhancement trend was observed in the ICL. Furthermore, the transmittance of both PEDOT:PSS and ICL demonstrated a sequential enhancement trend with increasing atomic number of the alkali metals (Fig. 2c). The thicknesses of pristine and AMC doped PEDOT:PSS layers were measured via atomic force microscopy (AFM) (Fig. 2d and Fig. S4). The optimal thicknesses for the pristine and doped PEDOT:PSS layers with Li_2CO_3, Na_2CO_3 and K_2CO_3 are 23, 20, 17 and 15 nm, respectively, which is consistent with the transmittance enhancement discussed above. To investigate the cause of the reduced PEDOT:PSS thickness with AMC doping, contact angle measurements were performed. As shown in the Fig. S5, the contact angle of PEDOT:PSS dispersion on the ZnO layer exhibits an increase trend from pristine to K_2CO_3-doped PEDOT:PSS. The decreased wettability of the PEDOT:PSS dispersion on ZnO is one of the main factors contributing to the thinner film thickness. The combined effect of reduced film thickness and enhanced transmittance directly facilitates photocurrent and PCE improvement in tandem devices. To further verify the necessity of AMC doping for performance enhancement, organic homo-TSCs were fabricated using an undoped PEDOT:PSS layer with a thin thickness of 15 nm. As shown in Fig. S6 and Table S2, although the J_{sc} increases, both the V_{oc} and FF decrease, indicating that a thinner undoped PEDOT:PSS layer is insufficient to effectively isolate the two active layers.

To investigate the influence of AMC doping on the work function of PEDOT:PSS layers, ultraviolet photoelectron spectroscopy (UPS) was conducted (Fig. 2e, f). The work function of PEDOT:PSS layers doped with AMCs were slightly decreased, with the lowest value of 5.01 eV for K_2CO_3 doped PEDOT:PSS. This negligible work function change wouldn't reduce the V_{oc} of the tandem device, as shown in Table 1, especially when an additional phosphomolybdic acid hydrate (PMA) [27–29] layer with high work function is modified on the PEDOT:PSS layer.

X-ray photoelectron spectroscopy (XPS) was performed to investigate the AMC doping effect on the PEDOT:PSS layer. As shown in Fig. S7, the signals of Li 1*s*, N 1*s* and K 2*p* peaks confirmed successful doping of AMCs. S 2*p* peaks were separately identifiable for the two primary components, where the XPS peaks between 162 and 166 eV belong to sulfur atoms in PEDOT, and XPS peaks between 166 and 172 eV come from sulfur atoms in PSS [30] (Fig. 3a). The gradually increased PEDOT peak compared with that of pristine PEDOT:PSS indicates a gradually higher PEDOT proportion in the films. By calculation, the PEDOT/PSS ratio indeed shows a gradually increased trend from pristine film (15 %) to K_2CO_3 doped film with the highest value of 19 % (Fig. 3b). This PEDOT/PSS ratio change may give rise to the phase separation between PEDOT and PSS induced by AMC doping [31,32]. The AMCs, which consist of alkali metal cations and carbonate anions, screen the charges on PEDOT and PSS, and interact specifically with negatively charged PSS chains and positively charged PEDOT chains, respectively [32]. This charge screening reduces the Coulombic attraction between PEDOT and PSS, leading to the phase separation between PEDOT and PSS. When a water-based solution is used, the water-soluble alkali metal PSS can be more readily removed from the substrate during the spin-coating process. This mechanism explains both the increased PEDOT/PSS ratio and the reduced film thickness with AMC doping. It is noted that higher PEDOT content can enhance the robustness of the film, effectively keeping the two subcells apart even when the PEDOT:PSS film is very thin (15 nm for K_2CO_3 doped film).

To gain more insight into the influence of AMC doping effect on the PEDOT:PSS layers, optical absorption and Raman spectra were carried out. Optical absorption results at optimal doping concentration (1 mM) show reduced trend compared with the pristine

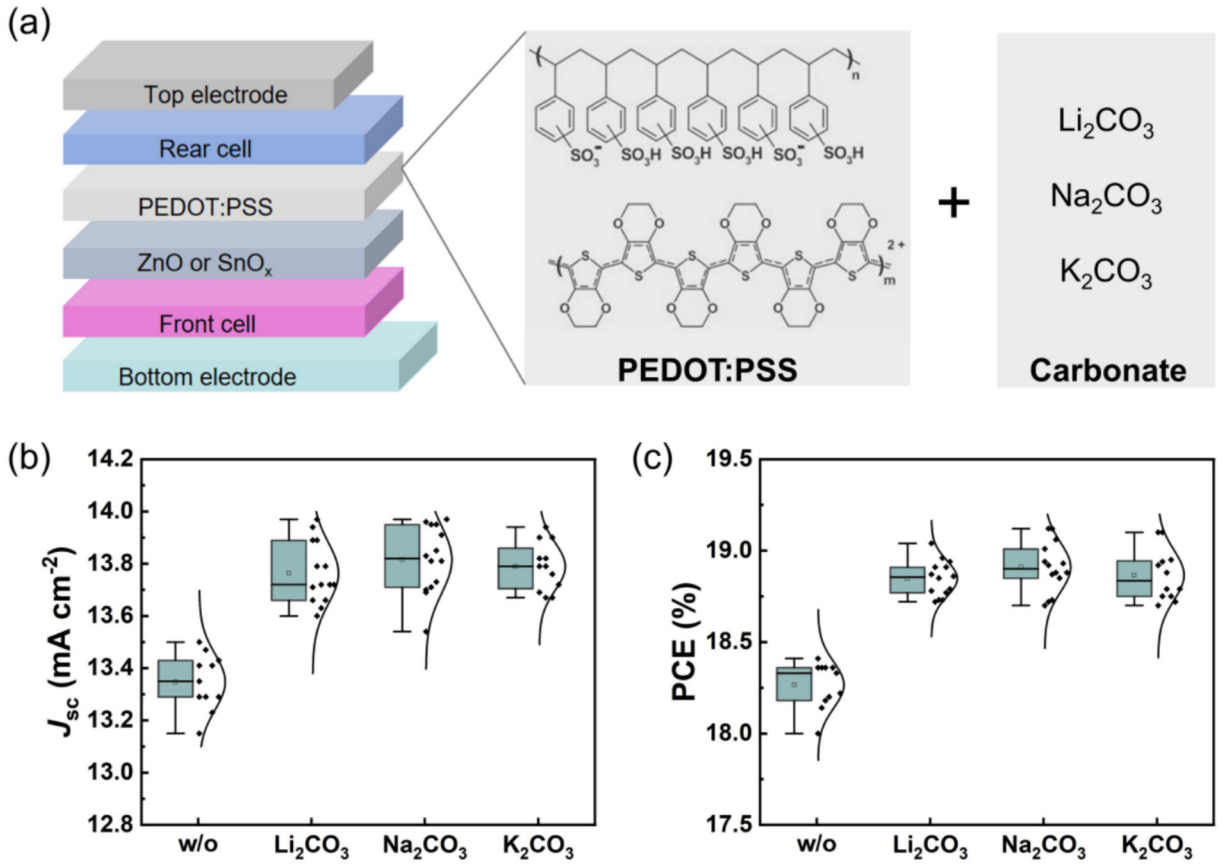

Fig. 1. (a) Basic device structure of tandem solar cells with metal oxide/PEDOT:PSS as interconnecting layer, chemical structure of PEDOT:PSS and the dopants. Statistics of (b) J_{sc} and (c) PCE in corresponding conditions for 11–14 individual devices.

Table 1
Photovoltaic parameters of PM6:CH22-based homo-TSCs under the illumination of AM 1.5 G, 100 mW cm^{-2}.

PEDOT:PSS	V_{oc}[a] (V)	J_{sc}[a] (mA cm^{-2})	FF[a] (%)	PCE[a] (%)
w/o	1.736 (1.730 ± 0.004)	13.41 (13.35 ± 0.10)	79.06 (79.15 ± 0.88)	18.41 (18.27 ± 0.12)
Li_2CO_3	1.733 (1.731 ± 0.002)	13.94 (13.76 ± 0.11)	78.83 (79.13 ± 0.49)	19.04 (18.85 ± 0.09)
Na_2CO_3	1.730 (1.730 ± 0.003)	13.95 (13.82 ± 0.12)	79.23 (79.09 ± 0.49)	19.12 (18.91 ± 0.13)
K_2CO_3	1.733 (1.730 ± 0.04)	13.90 (13.79 ± 0.09)	79.27 (79.07 ± 0.46)	19.10 (18.87 ± 0.13)

[a] The average values and standard deviations were obtained from statistical analysis of 11–14 individual devices.

PEDOT:PSS film (Fig. S8), which is consistent with the transmittance data above. While the small change in optical absorption is unable to estimate the doping state of different PEDOT:PSS layers. Fig. S9 depicted the absorption spectra at higher doping concentration (50 mM) of AMC. The absorption results exhibit a decrease in intensity in the near-infrared (NIR) region and an increase in intensity in the visible region, indicating a reduced doping level in the PEDOT:PSS [33]. The oxidation degree of PEDOT by AMC doping is also evident by Raman spectra (Fig. 3c and Fig. S10). All the films show a main peak between 1350 and 1500 cm^{-1}, corresponding to the $C_\alpha = C_\beta$ symmetrical stretching vibration on the PEDOT chain. The red-shifted peak position and narrowed spectra indicate that a dedoping process occurs from the pristine film to the K_2CO_3-doped film [34]. The dedoping process leads to a slight reduction in the vertical conductivity of the PEDOT:PSS films with AMC doping at 1 mM (Fig. 3f and Table S3). The detailed conductivity measurements can be found in the experimental section. This phenomenon parallels the conductivity reduction observed in sodium hydroxide-doped PEDOT:PSS, wherein increased doping concentration of AMC gradually increases pH values [35] (Fig. S11 and Table S4). Due to the reduction in film thickness after doping, the resistance of the PEDOT:PSS films itself does not increase relative to the pristine film (Fig. 3d, e), thus facilitating charge collection and transport. It should be pointed out that the compensatory effect between sequentially enhanced electrical resistance and optical transmittance across Li_2CO_3, Na_2CO_3 and K_2CO_3-doped PEDOT:PSS films lead to comparable photovoltaic performance in tandem devices (Fig. 3f).

To illustrate the reason of reduced conductivity of PEDOT:PSS films doped with AMCs, a possible mechanism is proposed. Due to hydrolysis, aqueous solutions of alkali metal carbonates exhibit alkalinity. This alkalinity induces the deprotonation of PSSH to PSS^-, which in turn reduces a portion of the highly doped PEDOT chains (enriched with bipolarons) to polarons and even to a neutral state [36]. Owing to the difference of alkali metal cation radius, the three cations exhibit different affinity for the PSS^- chains, with the largest K^+ possessing the weakest affinity. During the spin-coating process of the film itself and subsequent PMA alcohol solution, K^+ with weakest affinity is more readily removed, whereas most Li^+ remains in the PSS matrix. To balance the negative charge from

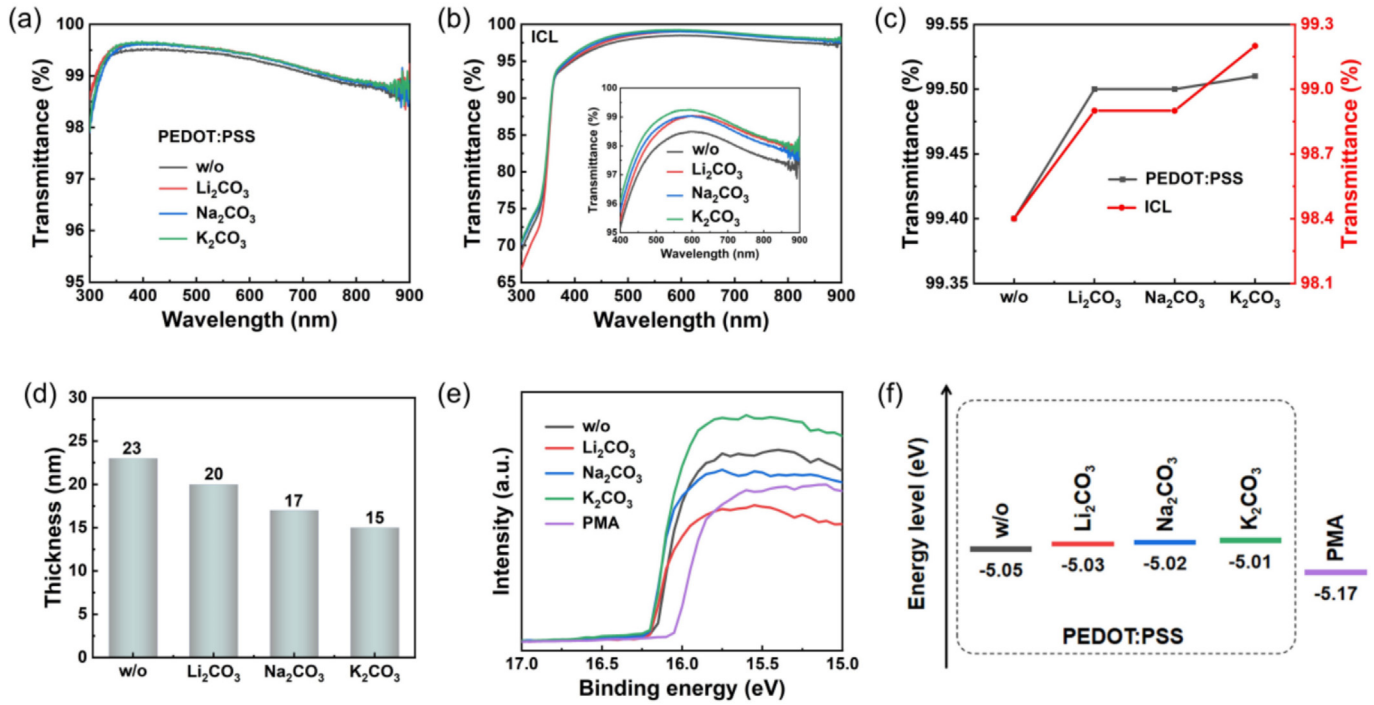

Fig. 2. (a) Transmittance spectra of PEDOT:PSS films. (b) Transmittance spectra of ICLs. (c) Transmittance values of PEDOT:PSS and ICLs with different AMC doping. (d) Thicknesses of PEDOT:PSS films. (e) UPS spectra of PEDOT:PSS films. (f) Work functions of PEDOT:PSS films and PMA layer. The doping concentration is maintained at 1 mM for all these AMC dopants.

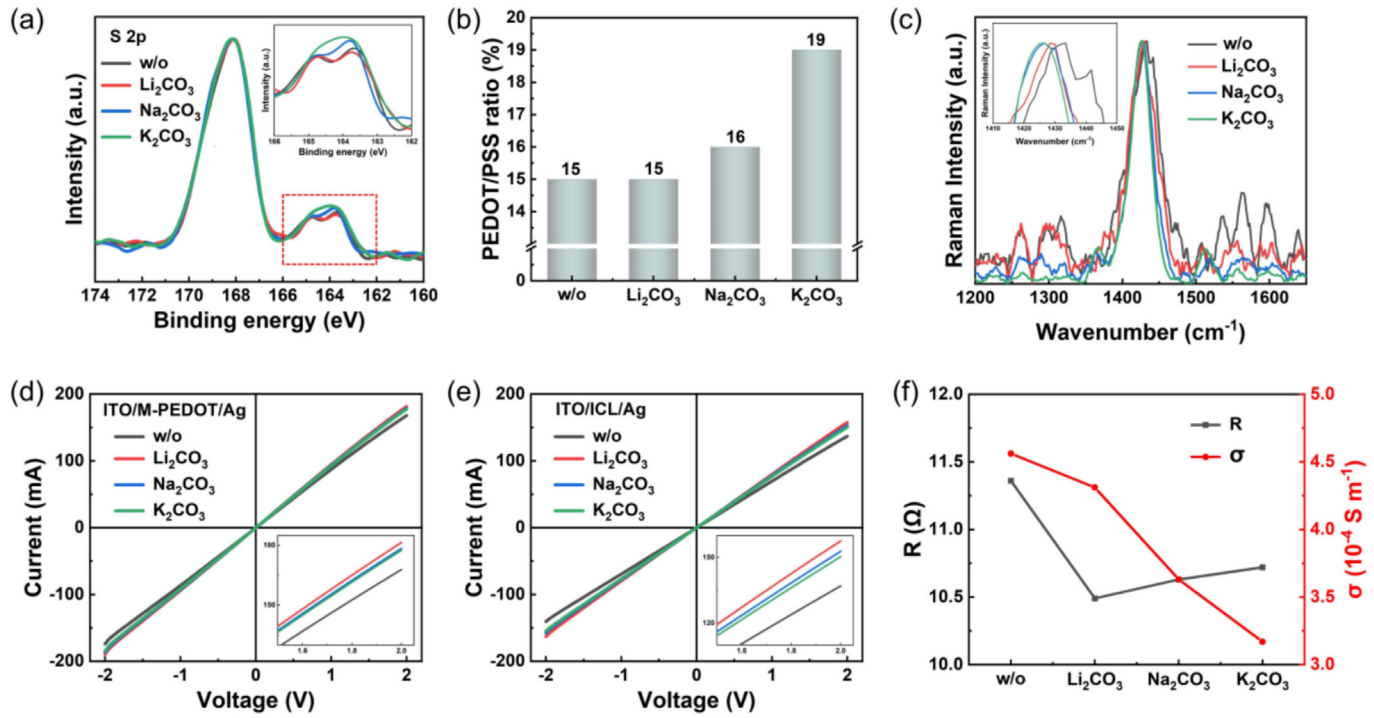

Fig. 3. (a) S 2*p* XPS spectra of PEDOT:PSS films. (b) Calculated ratios of PEDOT/PSS films. (c) Raman spectra of PEDOT/PSS films. (d) The current–voltage curves of devices with the structure of ITO/M-PEDOT (modified PEDOT:PSS)/Ag. (e) The current–voltage curves of devices with the structure of ITO/ICL/Ag. (f) Resistance and conductivity of PEDOT:PSS films with different AMC doping. The doping concentration is maintained at 1 mM for all these AMC dopants, except the Raman spectra (50 mM).

PSS^- after the alkali metal cations are removed, the p-type doped PEDOT chains will accept the electrons from PSS^- and become dedoped. This dedoping process explains the observed decrease in conductivity from pristine film to the K_2CO_3-doped film.

The surface morphology of these PEDOT:PSS films was measured via tapping mode AFM. As shown in Fig. 4, the PEDOT:PSS films are getting slightly rougher after AMC doping with 1 mM, with root-mean-square (RMS) roughness values of 0.86, 1.28,

1.27 and 1.23 nm for the pristine, Li_2CO_3, Na_2CO_3 and K_2CO_3-doped films, respectively. Rougher surface of AMC-doped PEDOT:PSS films could increase the surface area, which may facilitate the charge collection and suppress the charge recombination in the ICL. The degree of bimolecular recombination in the TSCs was evaluated using the relationship: $J_{sc} \propto (P_{light})^S$, where the exponential factor S value close to 1 implies weak bimolecular recombination in the device. Fig. S12 reveals that the AMC-based devices achieve relatively higher S values, conforming a reduction of bimolecular recombination. At high AMC doping concentration, the AFM image reveals obvious aggregation (Fig. S13), consistent with the proposed phase separation and the resultant decrease in device performance.

To validate the universality of AMC doping in PEDOT:PSS films, different active layer systems were employed to construct tandem devices by using Na_2CO_3 as a doping agent. As shown in the current density–voltage (J-V) curves (Fig. 5a, b), for homo-tandem organic solar cells based on PM6:L8-BO [37] and PM6:BTP-eC9 [38] as active layers, the J_{sc} has been obviously increased after doping with Na_2CO_3 for the PEDOT:PSS layer in the ICL. Since V_{oc} and FF remain relatively constant, the corresponding efficiencies are significantly improved. Notably, PM6:BTP-eC9-based homo-TSC achieves a high PCE of 20.04 %, which is among the highest reported values for homo-TSCs to date [25,39]. To compare with the other strategies reported previously, we also fabricated PM6:BTP-eC9-based homo-TSCs employing 2PACz-modified PEDOT:PSS layer as part of the ICL according to the previous work [25]. As shown in Fig. S14 and Table S5, this tandem device achieved a PCE of 19.41 %, which is consistent with the reported values [25]. However, compared to the Na_2CO_3-based tandem device, the 2PACz-based tandem device exhibits relatively lower J_{sc}. The enhanced device performance of the Na_2CO_3-based tandem device is attributed to the enhanced transmittance and decreased resistance of its ICL (Fig. S15). These results indicate that AMC doped-PEDOT:PSS leads to superior tandem device performance compared to the 2PACz modification.

Moreover, perovskite/organic TSCs are also tested for validating the universality of the AMC doping strategy. Besides subcell engineering [40–43], the ICL is critical to the performance of perovskite/organic TSCs. As shown in Fig. 5c, both the J_{sc} and PCE are increased with Na_2CO_3 doping for the PEDOT:PSS layer in the ICL, reaching a high PCE of 26.05 % with PM6:BTP-eC9 as the active layer of rear cell. Cross-sectional scanning electron microscopy (SEM) image (Fig. 5d) displays that the wide-bandgap perovskite (PVK) and PM6:BTP-eC9 active layers are distinctly separated by the ICL. Half-stacked TSCs with the structure of glass/FTO/front cell/ICL were assembled to investigate the optical transmission behavior in a more straightforward manner (Fig. 5e). As expected, the Na_2CO_3-based half-stacked-TSC demonstrates a slightly superior transmission in the 700–900 nm region, indicating that more near-infrared photons can reach the organic rear cell. Subsequently, external quantum efficiency (EQE) measurements are conducted to investigate the photon-to-electron conversion in the TSCs (Fig. 5f). While the EQE values for the front cells remain almost the same (14.47 and 14.48 mA cm^{-2}), the rear cell based on Na_2CO_3 doping exhibits a slightly enhanced response in the 700–900 nm region, increasing the EQE value from 14.35 to 14.52 mA cm^{-2}. This improvement in the rear cell's EQE value achieves better current balance between the subcells, which in turn boosts the J_{sc} of the tandem device from 14.32 to 14.70 mA cm^{-2}. The EQE curves are consistent well with the optical transmittance measurements. Therefore, these results indicate that the AMC doping strategy in PEDOT:PSS films exhibits good universality in TSC optimization.

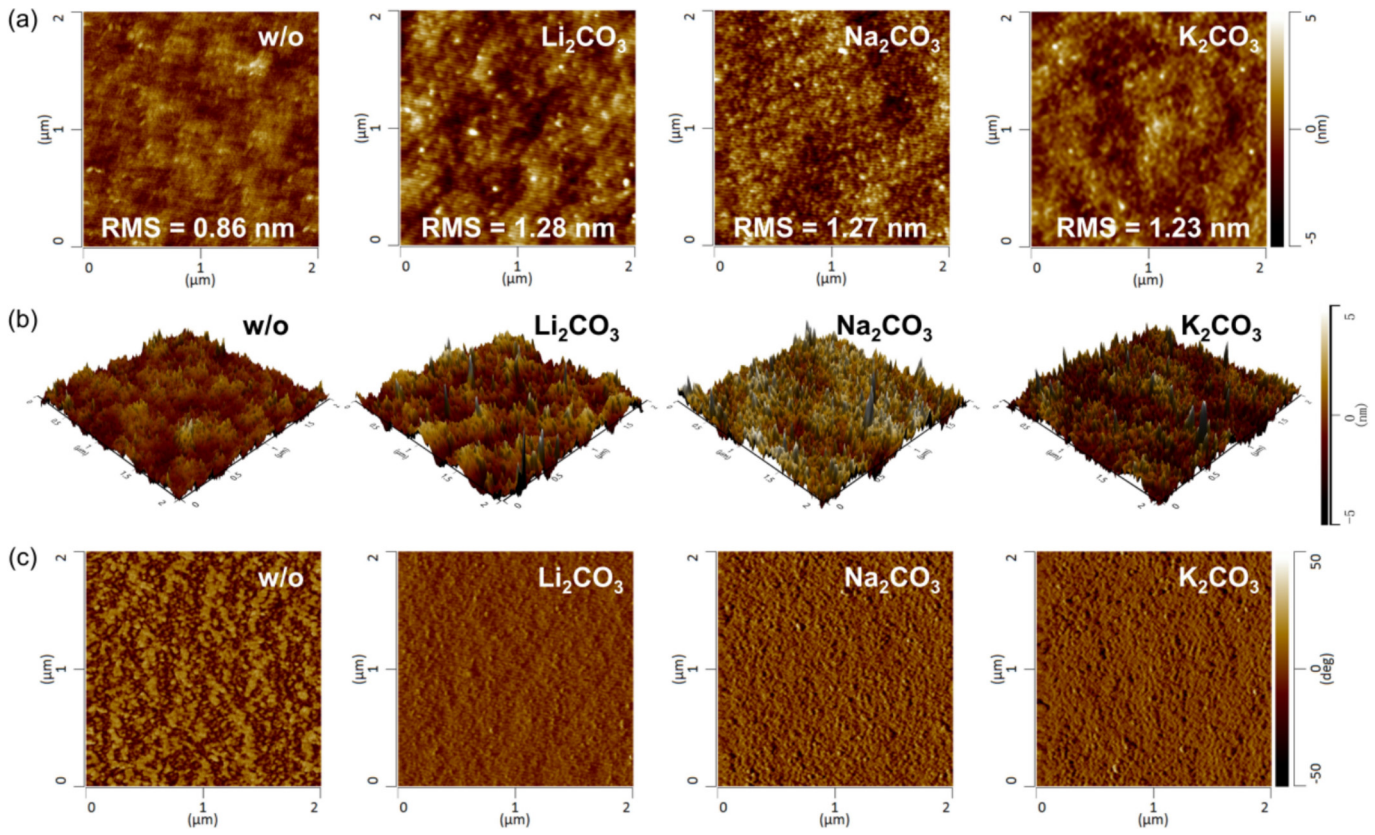

Fig. 4. AFM height images: (a) two-dimensional and (b) three-dimensional images. (c) AFM phase images of PEDOT:PSS films with different AMC doping. The doping concentration is maintained at 1 mM for all these AMC dopants.

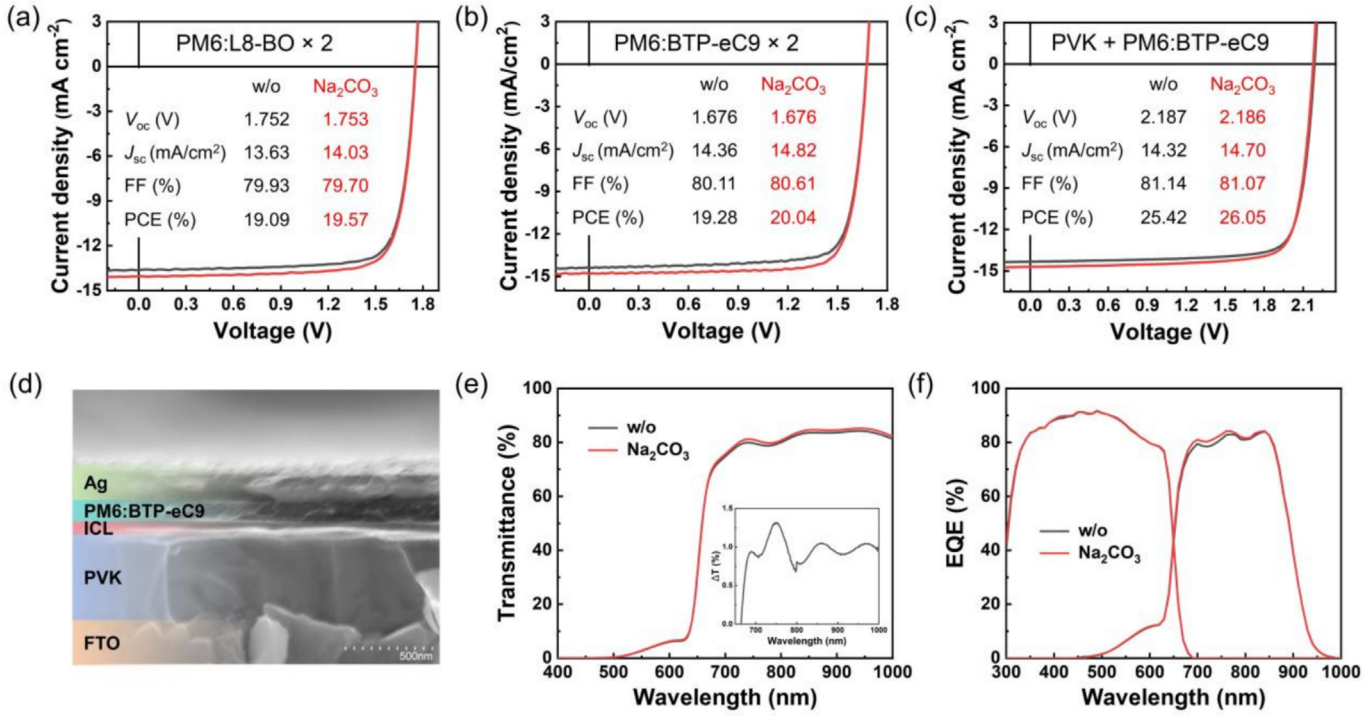

Fig. 5. *J-V* curves of organic homo-TSCs with (a) PM6:L8-BO and (b) PM6:BTP-eC9 as active layers. (c) *J-V* curves of perovskite/organic TSCs with PM6:BTP-eC9 as active layer of rear cell. (d) Cross-sectional SEM image of the optimal perovskite/organic TSC. (e) Transmittance spectra of half-stacked TSCs with the structure of glass/FTO/front cell/ICL. (f) EQE curves of perovskite/organic TSCs.

4. Conclusions

In conclusion, we develop an AMC doping strategy to reconstruct PEDOT:PSS film in the ICL and effectively enhance the performance of TSCs. XPS data implies that AMC doping can induce a gradually higher PEDOT proportion in the PEDOT:PSS films. This reconstruction makes the PEDOT:PSS films in ICLs to be ultra-thin but robust enough to protect front cell active layers from subsequent processing. Thin PEDOT:PSS films with AMC doping show decreased resistance along with a rougher surface, which jointly facilitates charge collection and transport. Consequently, this results in both J_{sc} and PCE enhancement for TSCs after AMC doping in PEDOT:PSS. Notably, AMC doping strategy in PEDOT:PSS films exhibits good universality in TSCs with different active layer combinations. PM6:BTP-eC9-based organic homo-TSCs achieve a high PCE of 20.04 %, which is among the highest reported values for homo-TSCs to date. Moreover, a high PCE of 26.05 % is obtained for perovskite/organic TSCs with PM6:BTP-eC9 as the active layer of rear cell. These findings underscore the great potential of AMC doping in optimizing PEDOT:PSS films in ICL, offering innovative pathways for fabricating various highly efficient TSCs.

CRediT authorship contribution statement

Bing Guo: Writing – review & editing, Writing – original draft, Validation, Methodology, Investigation, Formal analysis, Data curation, Conceptualization. **Ruihan Wu:** Methodology, Investigation. **Senyao Wang:** Methodology, Investigation. **Jiaqi Li:** Methodology, Investigation. **Bin Kan:** Methodology. **Zhaoyang Yao:** Writing – review & editing, Methodology. **Xiangjian Wan:** Methodology. **Chenxi Li:** Methodology. **Lei Meng:** Writing – review & editing, Methodology. **Yongfang Li:** Methodology. **Yongsheng Chen:** Writing – review & editing, Supervision, Project administration, Methodology, Investigation, Conceptualization.

Declaration of competing interest

The authors declare that they have no known competing financial interests or personal relationships that could have appeared to influence the work reported in this paper.

Acknowledgments

This work was supported by National Key R&D Program of China (2023YFE0210400) and the National Natural Science Foundation of China (62404222, 22479081, and 22361132530).

Appendix A. Supplementary material

Supplementary data to this article can be found online at https://doi.org/10.1016/j.jechem.2025.11.024.

References

[1] D. Di Carlo Rasi, R.A.J. Janssen, Adv. Mater. 31 (2019) 1806499.
[2] X. Xu, Y. Li, Q. Peng, Small Struct. 1 (2020) 2000016.
[3] M. De Bastiani, A.S. Subbiah, M. Babics, E. Ugur, L. Xu, J. Liu, T.G. Allen, E. Aydin, S. De Wolf, Joule 6 (2022) 1431–1445.
[4] G. Yang, C. Deng, C. Li, T. Zhu, D. Liu, Y. Bai, Q. Chen, J. Huang, G. Li, Nat. Photon. 19 (2025) 913–924.
[5] W. Wang, J. Wang, Z. Zheng, J. Hou, Acta Phys. Chim. Sin. 78 (2020) 382–396.
[6] D. Vos, J. Phys. D Appl. Phys. 13 (1980) 839–846.
[7] W. Shockley, H.J. Queisser, J. Appl. Phys. 32 (1961) 510–519.
[8] Z. Fang, Q. Zeng, C. Zuo, L. Zhang, H. Xiao, M. Cheng, F. Hao, Q. Bao, L. Zhang, Y. Yuan, W.Q. Wu, D. Zhao, Y. Cheng, H. Tan, Z. Xiao, S. Yang, F. Liu, Z. Jin, J. Yan, L. Ding, Sci. Bull. 66 (2021) 621–636.
[9] Y. An, N. Zhang, Q. Liu, W. Jiang, G. Du, D. Chen, M. Liu, X. Huang, T. Lei, Q. Qiu, F.R. Lin, X.C. Zeng, A.K.Y. Jen, H.-L. Yip, Nat. Commun. 16 (2025) 2759.
[10] X. Jiang, S. Qin, L. Meng, G. He, J. Zhang, Y. Wang, Y. Zhu, T. Zou, Y. Gong, Z. Chen, G. Sun, M. Liu, X. Li, F. Lang, Y. Li, Nature 635 (2024) 860–866.
[11] S. Kang, Z. Wang, W. Chen, Z. Zhang, J. Cao, J. Zheng, X. Jiang, J. Xu, J. Yuan, J. Zhu, H. Chen, X. Chen, Y. Li, Y. Li, Adv. Mater. 37 (2024) 2411027.
[12] Y. Han, J. Fu, Z. Ren, J. Yu, Q. Liang, Z. Xu, X. Xie, D. Li, R. Ma, M. Cao, Y. Sun, C. Yang, J. He, X. Chang, K. Liu, P.W.K. Fong, J. Huang, H. Liu, Z. Liu, D. Xu, L. Cheng,

J. Zhang, G. Yang, X. Lu, Y. Zhu, Q. Tai, Q. Lin, H. Hu, Y. Yang, G. Li, Nat. Energy 10 (2025) 513–525.
[13] Z. Zhang, W. Chen, X. Jiang, J. Cao, H. Yang, H. Chen, F. Yang, Y. Shen, H. Yang, Q. Cheng, X. Chen, X. Tang, S. Kang, X.-M. Ou, C.J. Brabec, Y. Li, Y. Li, Nat. Energy 9 (2024) 592–601.
[14] X. Wu, D. Zhang, B. Liu, Y. Wang, X. Wang, Q. Liu, D. Gao, N. Wang, B. Li, L. Wang, Z. Yu, X. Li, S. Xiao, N. Li, M. Stolterfoht, Y.H. Lin, S. Yang, X.C. Zeng, Z. Zhu, Adv. Mater. 36 (2024) 2410692.
[15] J. Tian, C. Liu, K. Forberich, A. Barabash, Z. Xie, S. Qiu, J. Byun, Z. Peng, K. Zhang, T. Du, S. Sathasivam, T.J. Macdonald, L. Dong, C. Li, J. Zhang, M. Halik, V.M. Le Corre, A. Osvet, T. Heumüller, N. Li, Y. Zhou, L. Lüer, C.J. Brabec, Nat. Commun. 16 (2025) 154.
[16] S. Liu, L. Hao, J. Yu, Y. Xu, Y. Dou, J. Xie, Y. Wang, K. Zhang, F. Huang, Y. Cao, ACS Nano 19 (2024) 748–759.
[17] S. Wu, Y. Yan, J. Yin, K. Jiang, F. Li, Z. Zeng, S.-W. Tsang, A.K.Y. Jen, Nat. Energy 9 (2024) 411–421.
[18] R. Lin, Y. Wang, Q. Lu, B. Tang, J. Li, H. Gao, Y. Gao, H. Li, C. Ding, J. Wen, P. Wu, C. Liu, S. Zhao, K. Xiao, Z. Liu, C. Ma, Y. Deng, L. Li, F. Fan, H. Tan, Nature 620 (2023) 994–1000.
[19] J. Wang, Y. Wang, J. Ren, P. Bi, H. Li, J. Dai, S. Zhang, J. Hou, Adv. Mater. (2025). https://doi.org/10.1002/adma.202510378.
[20] Z. Jia, X. Guo, X. Yin, M. Sun, J. Qiao, X. Jiang, X. Wang, Y. Wang, Z. Dong, Z. Shi, C.H. Kuan, J. Hu, Q. Zhou, X. Jia, J. Chen, Z. Wei, S. Liu, H. Liang, N. Li, L.K. Lee, R. Guo, S.V. Roth, P. Muller-Buschbaum, X. Hao, X. Du, Y. Hou, Nature 643 (2025) 104–110.
[21] X. Guo, Z. Jia, S. Liu, R. Guo, F. Jiang, Y. Shi, Z. Dong, R. Luo, Y.-D. Wang, Z. Shi, J. Li, J. Chen, L.K. Lee, P. Müller-Buschbaum, D.S. Ginger, D.J. Paterson, Y. Hou, Joule 8 (2024) 2554–2569.
[22] Z. He, R. Yu, Y. Dong, R. Wang, Y. Zhang, Z. Tan, Nat. Commun. 16 (2025) 1773.
[23] M.R. Fitzsimmons, B. Roose, Y. Han, T. Kang, Y.H. Chiang, C.S. Huang, Y. Lu, T.C. Yang, C. Chosy, S. Guan, M. Anaya, S.D. Stranks, ACS Energy Lett. 10 (2025) 713–725.
[24] L. Zhang, K. Yang, R. Chen, Y. Zhou, S. Chen, Y. Zheng, M. Li, C. Xu, X. Tang, Z. Zang, K. Sun, Adv. Electron. Mater. 6 (2019) 1900648.
[25] J. Yu, L. Hao, K. Zhang, J. Zheng, J. Zhang, Y. Xu, M. Dong, J. Xie, H. Li, X. Luo, F. Huang, Chem. Eng. J. 500 (2024) 156887.
[26] H. Liang, X. Bi, H. Chen, T. He, Y. Lin, Y. Zhang, K. Ma, W. Feng, Z. Ma, G. Long, C. Li, B. Kan, H. Zhang, O.A. Rakitin, X. Wan, Z. Yao, Y. Chen, Nat. Commun. 14 (2023) 4707.
[27] V.A. Kolesov, C. Fuentes-Hernandez, W.-F. Chou, N. Aizawa, F.A. Larrain, M. Wang, A. Perrotta, S. Choi, S. Graham, G.C. Bazan, T.-Q. Nguyen, S.R. Marder, B. Kippelen, Nat. Mater. 16 (2016) 474–480.
[28] L. Meng, H. Liang, G. Song, M. Li, Y. Huang, C. Jiang, K. Zhang, F. Huang, Z. Yao, C. Li, X. Wan, Y. Chen, Sci. China Chem. 66 (2023) 808–815.
[29] H. Liang, K. Ma, S. Ding, W. Zhao, X. Si, X. Cao, Z. Yao, T. Duan, G. Long, C. Li, X. Wan, Y. Chen, Adv. Energy Mater. 14 (2024) 2402370.
[30] D.C.M. Sarah, A. Spanninga, C. Zhan, J. Phys. Chem. C 114 (2010) 14998–15004.
[31] F. Wu, P. Li, K. Sun, Y. Zhou, W. Chen, J. Fu, M. Li, S. Lu, D. Wei, X. Tang, Z. Zang, L. Sun, X. Liu, J. Ouyang, Adv. Electron. Mater. 3 (2017) 1700047.
[32] Y. Xia, J. Ouyang, Macromolecules 42 (2009) 4141–4417.
[33] S. Garreau, J.L. Duvail, G. Louarn, Synth. Met. 125 (2021) 325–329.
[34] S. Garreau, G. Louarn, J.P. Buisson, G. Froyer, S. Lefront, Macromolecules 32 (1999) 6807–6812.
[35] H. Kim, S. Nam, H. Lee, S. Woo, C.-S. Ha, M. Ree, Y. Kim, J. Phys. Chem. C 115 (2011) 13502–13510.
[36] J. Dong, J. Liu, X. Qiu, R. Chiechi, L.J.A. Koster, G. Portale, Engineering 7 (2021) 647–654.
[37] C. Li, J. Song, H. Lai, H. Zhang, R. Zhou, J. Xu, H. Huang, L. Liu, J. Gao, Y. Li, M.H. Jee, Z. Zheng, S. Liu, J. Yan, X.K. Chen, Z. Tang, C. Zhang, H.Y. Woo, F. He, F. Gao, H. Yan, Y. Sun, Nat. Mater. 24 (2025) 433–443.
[38] Y. Cui, H. Yao, J. Zhang, K. Xian, T. Zhang, L. Hong, Y. Wang, Y. Xu, K. Ma, C. An, C. He, Z. Wei, F. Gao, J. Hou, Adv. Mater. 32 (2020) 1908205.
[39] Y. Xu, Y. Liao, W. Wang, Y. Wang, J. Wang, Z. Suo, F. Li, R. Wang, W. Ni, B. Kan, L. Meng, X. Wan, Y. Chen, J. Hou, M. Li, Y. Geng, Adv. Mater. 37 (2025) 2501653.
[40] F. Qiu, M.-H. Li, J. Wu, J.-S. Hu, J. Energy Chem. 89 (2024) 364–370.
[41] M.-H. Li, X. Ma, J. Fu, S. Wang, J. Wu, R. Long, J.-S. Hu, Energy Environ. Sci. 17 (2024) 5513–5520.
[42] M.H. Li, X. Gong, S. Wang, L. Li, J. Fu, J. Wu, Z. Tan, J.S. Hu, Angew. Chem. Int. Ed. 63 (2024) 202318591.
[43] Y. Dong, R. Yu, G. Su, Z. Ma, Z. He, R. Wang, Y. Zhang, J. Yang, Y. Gong, M. Li, Z. Tan, Adv. Mater. 36 (2024) 2312704.